Physics Publications

Physics

9-2012

High-Frequency Rapid B-Mode Ultrasound Imaging for Real-Time Monitoring of Lesion Formation and Gas Body Activity During High-Intensity Focused Ultrasound Ablation

Madhu Sudhan Reddy Gudur
University of Michigan-Ann Arbor

Ronald Kumon
Kettering University

Yun Zhou
University of Michigan-Ann Arbor

Cheri X. Deng
University of Michigan-Ann Arbor

Follow this and additional works at: https://digitalcommons.kettering.edu/physics_facultypubs

Part of the Physics Commons

High-frequency Rapid B-mode Ultrasound Imaging for

Real-Time Monitoring of Lesion Formation and Gas Body Activity during

High Intensity Focused Ultrasound Ablation

Madhu Sudhan Reddy Gudur[1], Ronald E. Kumon[1,2], *Member, IEEE,* Yun Zhou[1], *Member, IEEE,*

Cheri X. Deng[1], *Member, IEEE*

[1]Department of Biomedical Engineering, University of Michigan, Ann Arbor, MI, USA

[2]Current address: Department of Physics, Kettering University, Flint, MI, USA

[*]Corresponding author:

Cheri X. Deng, Department of Biomedical Engineering, University of Michigan, Ann Arbor, MI

48109-2099, Tel: 734-936-2855; Fax: 734-936-1095; email: cxdeng@umich.edu.

Abstract

The goal of this study was to examine the ability of high-frame-rate and high-resolution imaging to monitor lesion formation and gas-body activity during high-intensity focused ultrasound (HIFU). *Ex-vivo* porcine cardiac tissue specimens (n=24) were treated with various HIFU exposures (4.33 MHz, 77–130 Hz pulse repetition frequency (PRF), 25–50% duty cycle, 0.2–1 s, 2600 W/cm^2). Radiofrequency (RF) data (0.8 x 11 mm) from B-mode imaging were obtained before, during and after HIFU exposure at 77-130 Hz frame rates using a high-frequency ultrasound imaging system (Visualsonics Vevo 770, 55 MHz center frequency). The time history of changes in the integrated backscatter (IBS), calibrated spectral parameters, and echo-decorrelation parameters of the RF data relative to the initial values were assessed for lesion identification by comparing against gross sections. The best identification was achieved using temporal maximum IBS with +12 dB threshold (receiver-operating characteristic curve area 0.96). Transient gas-body activity was identified and tracked using frame-to-frame echo decorrelation. Macroscopic (mm-sized) cavities formed when the initial expansion rate of the gas bodies was at least 0.8 mm/s. Together these assessments provide a method for visualizing spatiotemporal evolution of lesion and gas–body activity and for predicting macroscopic cavity formation.

Keywords: HIFU Ablation, Cavitation, Tissue Expansion, Integrated Backscatter, Decorrelation, Spectrum Analysis, High-Frequency Ultrasound

I. INTRODUCTION

The use of high intensity focused ultrasound (HIFU) for clinical ablation therapy [1-3] is increasing due to its ability to noninvasively generate necrosis in targeted tissue volumes with minimal effects on surrounding and intervening tissue. The volume of tissue necrosis generated by HIFU exposure, or lesion, is determined by the spatiotemporal distribution of temperature increase induced by HIFU [4, 5]. To achieve better control of the ablation process, robust and effective imaging methods are needed for real-time monitoring of tissue changes during HIFU application. While magnetic resonance imaging (MRI) [6] and x-ray computed tomography [7] have been used as effective image guidance during ablation, monitoring with diagnostic ultrasound imaging has the advantage of relatively lower cost, higher portability, and high spatiotemporal resolution. During HIFU application, the exposed tissue exhibits changes in the acoustical properties such as sound speed, attenuation, and ultrasound backscatter due to protein denaturation, coagulation, gas-body formation, and other effects. While a variety of methods have been proposed to improve ultrasound imaging of HIFU ablation and lesion formation based on these changes, the method has not yet been established as a robust and consistent technique.

Small temperature changes ($<10°C$) can be estimated by tracking echo shifts [8] or changes in ultrasound backscatter [9-11] using a linear relationship between temperature change and echo shifts. However, when larger temperature changes occur and the tissue undergoes coagulative necrosis, these kinds of temperature estimation methods may break down. Tissue elasticity has also been exploited to evaluate tissue ablation [12-15] because thermal lesions exhibit increased stiffness, but lesion characterization via elastographic imaging is subject to degradation in the presence of gas bodies [16].

3

HIFU ablation can also induce changes in attenuation [17-19] and ultrasound backscatter [18-20] that can be used to detect lesion formation. Changes in integrated backscatter to monitor HIFU lesion formation have been studied with B-mode RF data acquisition in *ex vivo* bovine liver [18, 19] at an imaging frequency of 7.5 MHz. Tadpole-shaped lesions showed an increase in differential attenuation of up to 3.5 dB/MHz/cm and increase in accumulated differential IBS of up to 25–30 dB, although more precise definition of the lesion was obtained with the differential IBS image. A subsequent study with cavitation detection showed that the differential attenuation and IBS were coincident with increased broadband noise and subharmonic generation, with the largest changes coming with the most cavitation activity [19]. Hyperechoic regions formed in US B-mode images during HIFU exposure have been correlated with cavitation and was used to quantify the formation and growth of lesions *in-vivo* in pig tissues [21-23].

Spectral parameters of the backscattered RF ultrasound data are related to tissue properties like effective acoustic scatterer size and concentration [24] which can change as a result of HIFU exposure, Lesions induced by HIFU in *ex vivo* chicken breast and rabbit liver showed increased midband fit of 6 to 8 dB compared to surrounding non-ablated tissue [24, 25]. These increases are likely due to the increased backscatter from (1) gas bodies induced by HIFU exposure in the focal region and (2) changes in effective scatterer size due to coagulative necrosis. Spectral parameters have also been computed to characterize lesions induced by RF ablation in *ex vivo* bovine liver [26].

Recently, echo decorrelation has been proposed as means to identify lesion formation in radiofrequency (RF) ablation, with the potential benefits of reduced sensitivity to acoustic shadowing and tissue motion as compared to other methods [27]. Mapping and characterization

4

of RF ablated lesions in *ex vivo* liver tissue with temporal maximum decorrelation showed good performance when compared to temporal maximum integrated backscatter using RF data from B-mode ultrasound imaging [27, 28].

The gas bodies that often form during HIFU ablation can be caused by inertial cavitation, tissue degassing, and/or boiling due to increased temperature during HIFU exposure [29]. These gas bodies strongly scatter ultrasound and distort the HIFU beam, resulting in inefficient ablation of distal tissue segment [30] and altered lesion location, shape and size from the original treatment plan. The presence of gas bodies can also result in enhanced heating beyond thermoviscous absorption [31]. In some cases, due to the combined effect of high acoustic pressure and rapid heating, macroscopic cavities may be generated in tissue during ablation. To detect these gas bodies, various passive [21, 32-34] and active cavitation detection strategies [33, 35-37] have been proposed, including methods for spatial cavitation mapping to locate these gas bodies [38-40].

Previous studies have investigated the effect of ultrasound exposure parameters on lesion size in HIFU ablation in cardiac tissue [41, 42], the correlation between echocardiographic and histologic lesion size [43, 44], and the differences between acute and chronic lesions [45]. Ultrasound B-mode imaging [43] and "M2D-mode" (500 Hz frame rate) imaging [10] have been reported for real-time temperature monitoring in HIFU ablation but these studies were performed at frequencies of less than 10 MHz. Imaging at higher frequencies provides higher spatial resolution as well as wider bandwidth. Although with shorter penetration depth, high-frequency ultrasound imaging can be particularly useful for catheter-based ablation such as applications for interventional cardiology. A "MicroLinear" catheter using a 24-element, 14 MHz phased array with integrated RF ablation probe has been reported for forward-looking imaging [46]. Real-time

M-mode monitoring of lesion formation at 20 Hz line rate by combining a high-frequency (25–33 MHz) ultrasound transducer with an RF ablation electrode has also been developed as a proof-of-concept catheter system [47]. Our group has demonstrated the feasibility of M-mode and B-mode imaging with at a center frequency of 55 MHz in a preliminary study [48].

In this study, we focus on developing methods of high frequency, high frame rate B-mode ultrasound imaging to monitor formation of lesion and gas bodies during HIFU ablation using *ex vivo* cardiac tissue specimens. B-mode RF data were acquired and are analyzed using grayscale, integrated backscatter, calibrated spectral parameters, echo decorrelation to obtain time-evolving HIFU-monitoring parameters. By comparing against gross images, the best method(s) for lesion identification are assessed via receiver-operating characteristic (ROC) curves [49] (see Sec. II.D.1 for details). For gas-body identification, a frame-to-frame echo decorrelation method [27] is proposed to evaluate the dynamic local motion and the expansion rate of the gas bodies and to predict the formation of cavities during ablation.

II. MATERIALS AND METHODS

A. Experimental Setup, HIFU Exposures, and Transducer Calibration

The experimental setup consisted of a HIFU system and a high frequency ultrasound imaging system (Vevo 770, VisualSonics, Toronto, Canada). In a water tank, the HIFU transducer and a Vevo imaging probe (RMV 708, nominal 55 MHz center frequency, 20-75 MHz bandwidth [−6 dB], 4.5 mm focal distance, 1.5 mm depth of focus [−6 dB]) were perpendicularly and confocally aligned with the common focus placed within *ex vivo* porcine cardiac tissue specimens obtained from an abattoir (Fig. 1). All experiments were performed with specimens that were used within 96 hours of harvesting, with the tissue stored in

physiological saline solution at 4°C between experiments. The HIFU system consisted of a signal generator (33220A, Agilent, Santa Clara, CA, USA), power amplifier (75A250, Amplifier Research, Souderton, PA, USA), and spherically focused - HIFU transducer (custom-designed, Riverside Research Institute; 4.33 MHz center frequency, 40 mm diameter, 42 mm focal distance) and was used to generate pulsed exposures with 2600 W/cm^2 focal intensity and various pulse repetition frequencies (PRF) (77 Hz, 103 Hz, 130 Hz), duty cycles (25%, 50%) and exposure times (0.2 s, 0.6 s, 1 s). These HIFU exposure conditions were chosen so that variation in lesion size (1.5–3.5 mm in length) and macroscopic cavity size (0–2.5 mm in length) was obtained.

The HIFU transducer was calibrated using the following procedure. First, an ultrasound power meter (UPM-DT-10, Ohmic Instruments, Easton, MD, USA) was used to measure the total power output of the transducer at various drive voltages. Second, the focal beam pressure profile (6 dB radial width of 1.2 mm and 6 dB axial focal depth of 3.8 mm) were measured by scanning a needle hydrophone (0.635 mm diameter active element, NP10-1, Dapco NDT, Ridgefield, CT, USA) through the acoustic field. The spatial peak intensity was then calculated by correlating the integration of the beam profile with the total power. All acoustic intensities are quoted as free-field, spatial-peak temporal-average values, and the estimated error is ±5%.

B. Imaging and Data Acquisition

To achieve a high frame rate of imaging, short-time B-mode (STBM) imaging (B-mode imaging with a reduced window size of dimensions 0.8 mm x 11 mm) was employed. The STBM imaging was synchronized with the HIFU pulses to image during the off-duration of the HIFU pulses to avoid interference; thus the frame rate of STBM imaging was the PRF of the

pulsed HIFU exposure. Backscattered RF data of STBM imaging were acquired before, during and after HIFU application via the RF output port of the Vevo and a digitizing oscilloscope (Agilent 54830B, Santa Clara, CA, USA, with 8-bit dynamic range, 250 Ms/s). After the experiment, the tissue was cut transversely through the lesion and photographs of the lesion cross-section were taken.

C. Data Analysis

The following parameters were computed from the acquired RF data:

1) Grayscale (GS): The A-line signal acquired in STBM data was Hilbert transformed to obtain the complex analytic signal $p(y,z,t)$. (The conventional B-scan image is generally the logarithmic amplitude envelope of this signal, $\log_{10}|p(y,z,t)|$.) The grayscale parameter in decibels (dB) of a spatially smoothed frame at time t is calculated as

$$GS(y,z,t) = 10\log_{10}\left(\left\langle|p(y,z,t)|\right\rangle\right), \tag{1}$$

where the spatial smoothing with window $w(y,z)$ was defined by

$$\begin{aligned}\left\langle f(y,z)\right\rangle &= \iint w(y-y_0,z-z_0)f(y_0,z_0)dy_0dz_0\\ &= w(y,z)\otimes f(y,z)\end{aligned} \tag{2}$$

An isotropic Gaussian window

$$w(y,z) = e^{-\left(y^2+z^2\right)/2\gamma^2} \tag{3}$$

was used as the smoothing window represented in Eq. (2) with the length scale γ as 14 µm.

2) Integrated Backscatter (IBS): The auto-correlation function of a frame at time t is defined as

$$R_0(y,z,t) = \left\langle|p(y,z,t)|^2\right\rangle . \tag{4}$$

The position-dependent change in echo energy by integrated backscatter relative to the initial state, measured in decibels, is defined as [27]

$$IBS(y,z,t)=10\log_{10}\left(\frac{R_0(y,z,t)}{R_0(y,z,0)}\right),$$

(5)

where $R_0(y,z,0)$ is the temporal average of autocorrelation of the frames before HIFU ablation treatment. In this study, 0.02 s duration of data was collected in STBM format before HIFU treatment.

3) Frame-to-Frame Decorrelation: A spatiotemporal correlation function between two successive frames with a time delay τ is defined as [27]

$$R(y,z,t,\tau)=\left\langle p(y,z,t)p^*(y,z,t+\tau)\right\rangle.$$

(6)

The normalized frame-to-frame decorrelation parameter similar to the variance of the spectrum in "flow turbulence" denoted by Kasai et al. [50], is then defined as

$$\sigma_{FF}(y,z,t,\tau)=\left|\frac{2\left(R_0(y,z,t)-|R(y,z,t,\tau)|\right)}{R_0(y,z,t)+\overline{R_0}(t)}\right|,$$

(7)

where $\overline{R_0}(t)$ is the spatial mean of $R_0(y,z,t)$ for the frame obtained at time t.

4) *Initial Frame Decorrelation:* The initial frame decorrelation is defined as the decorrelation between any frame at time t and a frame at $t = 0$ (initial frame):

$$\sigma_{IF}(y,z,t)=\left|\frac{2\left(R_0(y,z,0)-|R(y,z,0,t)|\right)}{R_0(y,z,0)+\overline{R_0}(0)}\right|,$$

(8)

5) Spectral Parameters: The power spectrum of the STBM data was calculated for the signals of each RF A-scan within the ROI by taking the Fast Fourier Transform (FFT) of the data gated by a series of sliding Hamming windows of 0.2 μs, each offset by 0.1 μs. To remove

9

artifacts associated with the composite transfer function of the US system, calibrated power spectrum was obtained by dividing the tissue power spectrum by the calibration spectrum. The calibration spectrum was obtained from the reflection of the imaging pulse from the interface of deionized water and phenylated silicone oil (Dow Corning 710, Midland, Michigan, USA). This approach [51] was used because the low reflectivity of the liquid–liquid interface prevented signal saturation by the Vevo system. The resulting signal was corrected for the deviation of water-oil interface from ideal specular reflector for the attenuation of the pulse due to the water between the scanhead and interface (particularly above 30 MHz) using material parameters from the literature [52, 53].

The calibrated power spectra were characterized by linear regression to find the spectral parameters, i.e. the midband-fit $M(y,z,t)$, which is the value of the linear function evaluated at the midpoint of the -15 dB bandwidth, the slope $m(y,z,t)$, and the intercept $I(y,z,t)$. The relative change in the spectral parameters were computed to minimize the effects of variability in the initial state of the specimens, e.g., for midband fit, $\Delta M(y,z,t) = M(y,z,t) - M_0(y,z)$, where $M_0(y,z)$ is the temporal average value of the spectral parameter in the frames prior to application of HIFU.

D. Pixel Marking and Parametric Images

To display lesion and gas-body formation on the grayscale B-mode images, we decided to mark each pixel with a single color corresponding to each feature to obtain composite parametric images:

1) Lesion mask and lesion identification: To construct ROC curves between the post-HIFU frame of STBM data and the gross image, a binary mask for the lesion in gross image at

10

the STBM window location need to be identified. A general block diagram of the procedure for obtaining the binary mask for lesion is shown in Fig. 2A. First the outer edge of the lesion (e.g., cyan contour in Fig. 2B) was manually drawn on the gross image of the tissue specimen to indicate the area of necrosis. Then, to represent the STBM window location on gross image, the post-HIFU B-mode image which was registered with the STBM window location (white dashed lines in Fig. 2C), was overlaid on top of gross image to register common structural features such as lesion, cavity (if exists), and boundaries of the tissue. After registering the STBM window in the gross image (Fig. 2D), the lesion area was used to create a binary mask (Fig. 2E) for representing the necrosed area (i.e., 1 is necrosed tissue and 0 is non-necrosed).

The proposed parameters defined in Eq. (1) to (8) along with spectral parameters are evaluated on each frame of STBM data. For any given parameter $X(y, z, t)$ defined in Eq. (1) to (8), the temporal maximum of the parameter was also computed according to

$$X_{\max}\left(y,z,t_{0}\right)=\max_{t}\left(X\left(y,z,0\leq t\leq t_{0}\right)\right). \tag{9}$$

This functional form captures the overall time history of the parameter in an effort to account for the irreversible nature of the HIFU ablation process. By thresholding $X_{\max}\left(y,z,t_{0}\right)$ on the last frame of STBM data, when the entire lesion has formed, a binary mask was generated (where 1 is above the threshold and 0 is below the threshold) and compared with the mask from the gross lesion on a pixel-by-pixel basis. For a given threshold, each pixel was classified as true positive, false positive, false negative, and true negative, where the gross lesion was taken as the "true" state. By varying the threshold, we constructed the receiver operating characteristic (ROC) curve, or true positive fraction (fraction of lesioned pixels correctly classified as lesion) vs. false positive fraction (fraction of non-lesioned pixels incorrectly classified as lesion), and the accuracy curve, or ratio of the sum of true positive and true negative pixels over all image pixels.

For a parameter that acts as an ideal classifier, the area under the ROC curve would be one. For a totally random classifier, the ROC would lie along the diagonal and have area of 0.5.

To determine the best threshold for lesion identification, training datasets ($n = 16$) were selected randomly and sampled uniformly from a pool of datasets ($n = 24$) undergoing HIFU treatment at the various ultrasound conditions mentioned in Sec. II.A. The pixel-by-pixel classification was applied on training and test datasets (remaining datasets, $n = 8$), and overall ROC and accuracy curves were generated. This procedure was repeated over 100 trials to ensure that all data were considered during training, and the resulting ROC and accuracy curves were averaged over all trials. We chose the "optimal" threshold to be the parameter threshold value at maximum accuracy.

2) Identification of gas bodies: The frame-to-frame echo decorrelation parameter σ_{FF} can be used to capture rapid changes in successive frames, and hence this parameter is proposed to identify any newly-formed or actively moving gas bodies, including any active process involving the expansion of the tissue. Because no gas bodies are likely to exist within the tissue prior to the initiation of HIFU treatment, any parameter used for classification of gas-body activity should, at minimum, not identify gas bodies during the pre-HIFU period. For any given parametric image $\sigma_{FF,j}(y,z,t)$ of the jth specimen, the threshold $\sigma_{FF,j}^{0}$ for gas-body identification was chosen to be minimum value of σ_{FF} such that $\sigma_{FF,j}(y,z,t) < \sigma_{FF,j}^{0}$ for all y and z at all $t < t_{\text{ON}}$, where t_{ON} is the time of HIFU initiation. Note that the threshold $\sigma_{FF,j}^{0}$ of jth specimen is independent of others. After gas bodies were identified, the amount of the displacement of their top most pixel from the focal spot was tracked in each frame to evaluate the rate at which the cavity is expanding, defined as dynamic expansion rate (ER) of the cavity. A moving-average filter of duration 0.08 s was applied to the displacement of gas bodies to

remove the artifacts due to tissue movements that may have occurred during HIFU. After classifying each lesion as "cavity-forming" or "non-cavity-forming" based on the existence of macroscopic cavities in gross lesions, the expansion rate for each specimen was computed and then a threshold to segregate the two types of lesion was determined.

3) Composite image. To represent all features of ablation process in any given frame, a composite red-green-blue (RGB) image was constructed depicting lesion as red, gas-body activity at times when the expansion rate is below the cavity-forming threshold as green, and gas-body activity at times when the expansion rate is above the cavity-forming threshold as blue, with the intensity of each pixel determined by the grayscale $GS(y,z,t)$ value of the RF data. In this way, the entire evolution of the ablation process can be graphically displayed.

III. RESULTS

An example of high frequency, rapid B-mode imaging on a cardiac *ex-vivo* sample is presented in Sec. III.A. to show the spatiotemporal changes observed during HIFU ablation. Using this example, the process of lesion identification by various proposed parameters and selection of the best parameter for lesion identification are presented in Sec. III.B. In Sec. III.C, a proposed method of frame-to-frame decorrelation for identification and tracking of gas bodies and estimation of their expansion rate to aid the cavity formation prediction during the ablation are presented. Finally, the demonstration of lesion identification process, detection and tracking of gas bodies on three HIFU ablation examples of *ex-vivo* cardiac specimens are presented in image and video formats in Sec. III.D.

A. High Frequency Rapid B-mode Imaging during HIFU Ablation

Figure 3 shows an example for HIFU ablation (4.33 MHz center freq., 2600 W/cm^2, 77 Hz PRF, 50% duty cycle and 1 s exposure time) illustrating the complex dynamic changes in tissue during HIFU exposure involving tissue necrosis and formation of gas bodies. With the HIFU beam incident from the left side of the image, the B-mode image after HIFU (Fig. 3B) clearly shows the lesion compared with the image before HIFU (Fig. 3A), and matches very well with the gross image of the lesion (Fig. 3C). The dashed vertical lines indicate the lateral boundaries of the short time, B-mode (STBM) window. While the spatiotemporal evolution of the lesion can be more readily appreciated in the video playback of the STBM frames, the horizontally stacked images are included in Fig. 3D for convenient representation. Selected frames from Fig. 3D are enlarged to better show the dynamics of HIFU lesion and gas body evolution in detail in Frames $3F_1$–F_{11}. After the HIFU is turned on at $t = 0.02$ s, a bright hyperechoic region appeared near the focus after a time delay at $t = 0.16$ s, most likely representing gas-body activity generated by acoustic cavitation and thermally induced water vaporization at the 2600 W/cm^2 intensity [33] and the relatively high frequency of the HIFU transducer used in this study. The initiation of gas-body activity is clearly shown starting from the left side in Frame $3F_2$ (closer to the HIFU transducer) and then growing in subsequent Frames $3F_3$–F_4 before filling the entire width of the window by Frame $3F_6$. The hyperechoic region appears to grow and expand laterally with respect to the HIFU beam axis (Frame $3F_7$). This lateral expansion of the hyperechoic region could be due to the combined effects of apparent echo strain resulting from variation in speed of sound at elevated temperatures and thermal expansion of the tissue. After the HIFU is turned off, the bright regions move downward (away from the imaging transducer), indicating contraction and maybe dissipation of the gas bodies (Frames $3F_8$ and $3F_9$) and two weakly echogenic regions become visible, separated by a

hypoechoic region in between (Fig. 3D and Frames $3F_8$ and $3F_9$). These hyperechoic and hypoechoic regions from STBM (indicated by the white vertical dashed lines) correspond well with the tissue necrosis and cavity regions of the gross tissue image (Fig. 3E) (same as Fig. 3C). Fig. 3E also highlights the contour (cyan line) manually drawn along the outer edge of the lesion to indicate the area of necrosis.

B. Lesion Identification

From the gross image (Fig. 3E), the STBM window was isolated and used to determine a mask representing the necrosed area. The various parameters described in Sec. II.C and their temporal extrema were then computed for each frame in the B-mode series. By applying a threshold to the final frame, accuracy of the parameter for lesion identification at that threshold was determined.

By applying this procedure to all the data sets, an overall ROC curve was generated for each parameter (Fig. 4). The ROC area under the curve (AUC), maximum accuracy, optimal threshold at maximum accuracy, sensitivity, and specificity from pixel-by-pixel classification for each parameter is shown in Table 1. IBS_{max} and ΔM_{max} have highest areas under the ROC curve (ROC AUC ~ 0.96). We chose to compute IBS_{max} for subsequent analysis as it had the highest AUC. In contrast, grayscale thresholding performs significantly worse for lesion detection (ROC AUC = 0.66). The standard deviation shown for AUC was calculated using all 24 datasets.

The training data sets ($n = 16$) attain maximum accuracy in detecting the lesion at an IBS_{max} of +12 dB. When the threshold for detecting the lesion is evaluated on the remaining test dataset group ($n = 8$), the predictive measures such as accuracy, sensitivity and specificity obtained are presented in Table 2 along with the results for training and entire dataset groups.

15

The small difference in predictive measures between training and test datasets indicates that the performance of IBS_{max} was not strongly affected by the choice of training datasets. Thus, for all ablation types with ultrasound conditions specified in Sec. II.A, an accuracy of 93.5% is achieved using IBS_{max} in matching the lesion area with gross tissue specimen.

C. Identification and Tracking of Gas Bodies

The mean and standard deviation of the frame-to-frame echo decorrelation thresholds for gas-body formation based on pre-HIFU frames were $\sigma_{FF}^0 = 2.5 \pm 0.6$. Once identified, the movement of the gas bodies can then be tracked in the STBM images. As an example, Fig. 5 shows a series of stacked short time B-mode frames with gas-body activity marked in green, as identified by frame-to-frame echo decorrelation method. The top-most pixel in each frame that is identified as gas-body activity (if there exists one) is represented by red dot to track its location in time. Cases where pronounced movement/expansion of the tracked gas bodies occurred (Fig. 5A) were well correlated with the existence of macroscopic cavity formation during HIFU as shown in gross image (Fig. 5B, the case in Fig. 2), in contrast with minimal movement of gas bodies for cases where no observable macroscopic cavity was generated (Fig. 5C and 5D) (2600 W/cm^2, 77 Hz PRF, 50% duty cycle and 0.2 s exposure time).

Figure 5E shows the displacements tracked in Fig. 5A and C along with the corresponding smoothed curves. The lateral expansion of the gas bodies is much more pronounced in the case when cavity was generated by higher HIFU intensity and longer exposure (Fig. 5A and B). The corresponding expansion rate (ER) of the top-most gas-body location (Fig. 5F), computed by taking the numerical derivative of the moving average curves in Fig. 5E, also show much higher values. The expansion of the cavity is rapid until 0.6 s, and most of the

expansion occurs by 0.8 s, reaching a near maximum expansion for the HIFU exposure condition. Correspondingly, the ER of the gas bodies in Fig. 5E rises, attaining a maximum around 0.35 s, while the ER is near zero for the case without cavity found in the gross image of tissue. These observations suggest that a high value of initial ER of gas-body activity may be precursor of macroscopic cavity formation.

To test this observation, the ER was calculated on all 24 data sets, 5 of which had a lesion but no cavity in the gross images. Fig. 6 shows that the non-cavity datasets have a significantly lower ER (0.51 ± 0.21 mm/s) compared to the cavity datasets (1.37 ± 0.39 mm/s) based on a T-test ($p < 10^{-4}$). As a result, the threshold of 0.8 mm/s was chosen to classify those gas bodies associated with cavity formation based on the maximum ER value among the non-cavity data sets.

D. Parametric Imaging for Lesion and Gas Body Marking during HIFU Ablation

Using the criteria for identification of lesion and gas bodies developed in Secs. B and C, parametrically-labeled images were generated retrospectively to demonstrate the feasibility of tracking lesion and gas-body formation during HIFU exposure. The results were examined for different HIFU exposure conditions ablation cases where different gas-body dynamics might be expected.

For the data of Fig. 2, Fig. 7 shows selected grayscale image frames with markings for the lesion, gas-body activity, and cavity-formation superimposed. (The video playback of all composite RGB frames is shown in **Media-Movie 1**.) Consecutive frames are separated by white dashed vertical lines and others by blue dashed lines. Frame $7A_1$ shows the last frame prior to HIFU application, with the early evolution of the lesion (red) after the initiation of gas-body

17

activity shown in Frames $7A_2$–A_5. The ER of the gas bodies is below the threshold until Frame $7A_5$, and these gas bodies are represented in green. At 0.299 s (Frame $7A_6$), the ER crosses the threshold, indicating the capability of the gas bodies to create a cavity, and reaches a maximum ER of 1.36 mm/s at 0.377 s (Frame $7A_9$). The gas bodies in Frames $7A_6$–A_{17} are then color coded in blue. The gas body expands, and the lesion grows until Frame $7A_{13}$ when the HIFU is turned off. Frames $7A_{14}$–A_{16} show a downward movement, representing shrinking and dissipation of the gas-body activity. The lesion-marking algorithm covers most of the area of lesion contour (cyan curve) determined from the gross lesion, although lesion extent is over-estimated in the region below the lesion. This overestimation is likely due to reverberation artifacts of the backscattered ultrasound from the HIFU-induced gas body, as seen in Frames $7A_{10}$ and $7A_{12}$.

Effect of PRF. Figure 8 shows an example of a case with HIFU ablation at higher PRF than in Fig. 7 (130 Hz vs. 77 Hz) with all other conditions equal. A cavity apparent in the B-mode image after HIFU treatment (Fig. 8A) is confirmed in the gross image (Fig. 8B). The extent of lesion area (red) predicted from STBM data using IBS_{max} with +12 dB threshold is overlaid on STBM window of the post-HIFU B-mode image (Fig. 8C). As shown in Fig. 8D, selected frames from the time evolution of the ablation, higher PRF ablation generates less area identified as gas and a smaller cavity size in the gross tissue as compared to Fig. 7. The ER crossed the cavity-formation threshold at 0.492 s (frame $8D_7$), reaching a maximum ER of 1.35 mm/s at 0.515 s (frame $8D_8$), and then dissipation of gas bodies occurred after the HIFU was turned off. When the cases with 77 Hz and 130 Hz PRF are compared (2600 W/cm^2, 50% duty cycle), the durations for crossing the ER threshold after HIFU was turned on were 0.324±0.090 s ($n = 8$) and 0.405±0.054 s ($n = 4$), respectively, although the difference was not

quite statistically significant (T-test with unequal variances, $p = 0.077$). The increased delay illustrated in Fig. 8 as compared to Fig. 7 suggests that higher PRF may result in slower expansion. This slower growth of gas bodies could be the reason for smaller cavity size (cavity area = 0.089 ± 0.069 mm^2, $n = 4$ for 130 Hz vs. 0.187 ± 0.064 mm^2, $n = 4$ for 77 Hz with other conditions 2600 W/cm^2, 50% duty cycle and 1 s exposure time being same) at the end of the ablation as seen in the gross image (Fig. 8B).

Effect of Exposure Duration. Figure 9 shows an example of a dataset with lower exposure duration than in Fig. 7 (0.2 s vs. 1.0 s) with all other conditions equal. (See **Media-Movie 2** for the corresponding video.) The B-mode image shown in Fig. 9A does not show any hypoechoic regions without the presence of a macroscopic cavity in the lesion (Fig. 9B). The predicted lesion area (red) from STBM data is overlaid on STBM region of post HIFU B-mode image (Fig. 9C). Figure 9D shows a composite image that presents the evolution of the ablation process with time. Although sudden occurrence of gas bodies (Frame 9D$_3$) and their initial activity (Frames 9D$_3$–D$_5$) was observed, the short HIFU exposure duration limited the chance for the expansion/movement of these gas bodies and formation of a tissue cavity. (At Frame 9D$_6$ the HIFU was turned off.) Because the ER of the gas bodies did not cross the threshold, they remain colored in green. In the datasets with lower HIFU exposure times (with all other conditions equal: 2600 W/cm^2, 77 Hz PRF, 50% duty cycle), the cavity was either absent (0.2 s exposure, $n = 5$) or small (cavity area = 0.066 ± 0.039 mm^2 for 0.6 s exposure, $n = 6$) compared to Fig. 7 (cavity area = 0.187 ± 0.064 mm^2 for 1 s exposure, $n = 4$). The non-cavity datasets (all of which were 0.2 s exposure cases and without cavity in the gross images) in Fig. 6 were used to determine the ER threshold in the model so that no cavity is predicted in those datasets. For the datasets with 0.6 s and 1 s exposure, the maximum ERs (1.4 ± 0.2 mm/s vs. 1.5 ± 0.3 mm/s) and

their time of occurrence (0.44 ± 0.04 s vs. 0.42± 0.04 s) were nearly the same. However, the total expansion was higher in the cases with longer exposure, resulting in a larger cavity size.

IV. DISCUSSION

A. Lesion Identification

Integrated backscatter, spectral parameters, and echo decorrelation have been explored in estimating the formation of lesion area in previous work.

Integrated backscatter. The approach of changes in integrated backscatter (IBS_{max}) has been used previously to monitor HIFU lesion formation with B-mode RF data acquisition in *ex vivo* bovine liver [18, 19], although at lower imaging frequency of 7.5 MHz. The authors observed sudden increases in the apparent width of the lesion midway through the exposure period, similar to the results observed at the longer exposure times in the current study (e.g., Fig. 7). A subsequent study with cavitation detection showed that the largest changes in IBS were associated with the cavitation activity [19]. The current study also observed abrupt increase in IBS when gas bodies were identified by the echo decorrelation method. The current method showed that the temporal maximum IBS performed better than the IBS alone in identifying the extent of the lesion as compared to the final state. However, the current method does appear to be affected by reverberation artifacts when extensive gas body formation occurs (Fig. 7, 8).

Spectral parameters. The ΔM and ΔI increases observed in lesions induced by HIFU of current study are consistent with other studies [24, 25], where an increase in midband fit of 6 to 8 dB in lesion over surrounding non-ablated tissue was observed in *ex vivo* chicken breast and rabbit liver. The slope parameter Δm in the current study yielded inconsistent results from case to case and was not useful for lesion identification (see Table 1). Spectral parameters have also

20

been computed to characterize lesions induced by RF ablation in *ex vivo* bovine liver [26]. The AUC ROC for intercept and midband fit were reported to be 0.71 and 0.69, respectively, which are comparable to values found in the current work (ΔI : 0.737, ΔM : 0.745), but worse than values for the corresponding temporal extrema (ΔI_{max} : 0.903, ΔM_{max} : 0.947) in Table 1. The improved ROC performance of ΔM_{max} and ΔI_{max} suggest that the usage of ablation time history via the temporal maximum method can increase the performance of these parameters for lesion identification.

Echo decorrelation. In the current study, IBS_{max} showed slightly better performance in lesion identification (ROC AUC 0.949) as compared to $\sigma_{FF,max}$ (ROC AUC 0.917), although the performance of $\sigma_{FF,max}$ was comparable to the previous study [27, 28]. The difference in the performance of IBS_{max} in the current study from [27] could be due to higher bandwidth, the increased backscatter due to HIFU-induced gas body formation, and higher imaging rate (77–130 Hz vs 50 Hz), which might allow IBS_{max} to capture faster activities and events.

To check the importance of high imaging frame rate on the performance of IBS_{max} in identifying the lesion, the frame rate of each dataset was manually decimated to half the original frame rate. Upon generating the IBS_{max} ROC curves of these decimated frame rate datasets, a drop in the ROC AUC (area under curve) by 20%, accuracy by 2%, and the sensitivity by 20% was observed. The drop is more prominent in the case when frame rate was reduced from 130 Hz to 65 Hz than in the case of 77 Hz to 39 Hz indicating that higher frame rate indeed improves the lesion identification by capturing faster events.

B. Gas Body Identification

Because of the gas-body formation significantly enhances echogenicity in the lesion region and $\sigma_{FF,\max}$ performed well in the identification of lesion extent, we proposed the use of frame-to-frame echo decorrelation σ_{FF} as a means to identify newly formed and expanding gas-body activity. The method will not capture pre-existing static gas bodies and hence cannot be used to map the location of all gas bodies (which is not the focus of the paper) during ablation. Based on the identified gas bodies, expansion rate information of the gaseous region was used to predict the occurrence of the macroscopic cavity.

The effects of various HIFU exposure parameters on the expansion rate of gaseous regions and the time to reach the threshold for macroscopic cavity formation were examined in this study. As described in the Sec. D, at higher PRF (130 Hz vs. 77 Hz) with other conditions equal, slower growth rate and smaller cavity size were observed. This is likely due to the shorter duration of each pulse. With reduced energy input in tissue during each ultrasound pulse, higher PRF reduced the likelihood of gas-body initiation and heating, thereby lowering the expansion rate. Consistent with this observation, in the data sets with lower duty cycle (25%, all other conditions equal: 2600 W/cm^2, 77 Hz PRF, 1 s exposure), a lower value of the maximum ER of 0.93 ± 0.02 mm/s ($n = 2$) was observed, compared to 1.5 ± 0.3 mm/s ($n = 4$) in the cases with 50% duty cycle. There was also a longer delay (0.68 ± 0.25 s) in reaching the maximum ER compared to that in the cases with 50% duty cycle (0.36 ± 0.12 s). The lower duty cycle exposure also resulted in smaller cavity sizes (cavity area $= 0.013 \pm 0.0014$ mm^2 at 25% duty cycle vs. cavity area $= 0.187 \pm 0.064$ mm^2 at 50% duty cycle) in the gross images at the end of ablation. These observations indicate that pulsed HIFU exposure parameters may be optimized to control gas-body activity in HIFU ablation.

Because the generation of macroscopic cavities in bulk tissue volumes may not be desired in achieving controlled HIFU ablation of cardiac tissue, identification of the precursors of such events can provide feedback control and adjustment of HIFU exposure parameters during treatment.

C. Study Limitations

In this study, lesion classification relied on matching the plane of B-mode imaging with the sectioning plane of the tissue lesion. Hence, small errors due to this mismatch in B-mode and gross tissue planes might occur in the estimation of lesion formation. Fixation and embedding of the tissue could allow for more precise sectioning but this process also introduces potential spatial distortion due to the tissue preparation process. In the spectral methods, the spatial averaging inherent in the method limits the spatial resolution over which the spectral parameters can be computed. The proposed criterion for gas-body identification was not corroborated with independent measurements (e.g., passive cavitation detection), and additional work is needed to better establish the relationship between echo decorrelation and gas-body formation. Finally, the acoustic radiation force can cause some tissue motion at the focal spot of HIFU probe during the treatment process; however, this effect was minimized by physically securing the tissue in place during ablation and by taking a moving-window time average of the displacement of gas bodies during estimation of ER.

V. CONCLUSION

Based on the RF data acquired from high-frequency, short-time B-mode imaging, we established a threshold to identify lesion area based on the time history of integrated backscatter.

In addition, we proposed frame-to-frame echo decorrelation to identify the rapidly-changing hyperechoic regions observed in the B-mode frames during ablation that are likely to be HIFU-induced gas-body activity. Based on this approach, we evaluated cavity expansion rate to develop a criterion for predicting the occurrence of a macroscopic cavity at the end of ablation. This criterion could be useful in situations where monitoring is needed to prevent macroscopic cavity formation in the HIFU treatment process.

REFERENCES

[1]   J. E. Kennedy, "High-intensity focused ultrasound in the treatment of solid tumours," *Nature Reviews: Cancer,* vol. 5, pp. 321-7, 2005.

[2]   M. A. Groh, O. A. Binns, H. G. Burton, 3rd *et al.*, "Ultrasonic cardiac ablation for atrial fibrillation during concomitant cardiac surgery: long-term clinical outcomes," *Annals of Thoracic Surgery,* vol. 84, pp. 1978-83, 2007.

[3]   G. ter Haar, "Harnessing the interaction of ultrasound with tissue for therapeutic benefit: High-intensity focused ultrasound," *Ultrasound in Obstetrics and Gynecology,* vol. 32, pp. 601-4, 2008.

[4]   C. Damianou and K. Hynynen, "The effect of various physical parameters on the size and shape of necrosed tissue volume during ultrasound surgery," *J Acoust Soc Am,* vol. 95, pp. 1641-9, 1994.

[5]   S. J. Graham, L. Chen, M. Leitch *et al.*, "Quantifying tissue damage due to focused ultrasound heating observed by MRI," *Magnetic Resonance in Medicine,* vol. 41, pp. 321-328, 1999.

[6]   K. Hynynen, A. Darkazanli, E. Unger *et al.*, "MRI-guided noninvasive ultrasound surgery," *Medical Physics,* vol. 20, pp. 107-115, 1993.

[7]   R. Yang, K. K. Kopecky, F. J. Rescorla *et al.*, "Sonographic and computed tomography characteristics of liver ablation lesions induced by high-intensity focussed ultrasound," *Investigative Radiology,* vol. 28, pp. 796-801, 1993.

[8]   C. Simon, P. Vanbaren, and E. S. Ebbini, "Two-dimensional temperature estimation using diagnostic ultrasound," *IEEE Trans Ultrason Ferroelectr Freq Control,* vol. 45, pp. 1088-99, 1998.

[9]   A. N. Amini, E. S. Ebbini, and T. T. Georgiou, "Noninvasive estimation of tissue temperature via high-resolution spectral analysis techniques," *IEEE Trans Biomed Eng,* vol. 52, pp. 221-8, 2005.

[10]   D. Liu and E. S. Ebbini, "Real-time 2-D temperature imaging using ultrasound," *IEEE Trans Biomed Eng,* vol. 57, pp. 12-6, 2010.

[11]   R. M. Arthur, D. Basu, Y. Z. Guo *et al.*, "3-D in vitro estimation of temperature using the change in backscattered ultrasonic energy," *IEEE Trans Ultrason Ferroelectr Freq Control,* vol. 57, pp. 1724-1733, 2010.

[12]   F. L. Lizzi, R. Muratore, C. X. Deng *et al.*, "Radiation-force technique to monitor lesions during ultrasonic therapy," *Ultrasound Med. Biol.,* vol. 29, pp. 1593-605, 2003.

[13]   R. Souchon, G. Bouchoux, E. Maciejko *et al.*, "Monitoring the formation of thermal lesions with heat-induced echo-strain imaging: A feasibility study," *Ultrasound Med. Biol.,* vol. 31, pp. 251-259, 2005.

[14]   C. Maleke and E. E. Konofagou, "Harmonic motion imaging for focused ultrasound (HMIFU): a fully integrated technique for sonication and monitoring of thermal ablation in tissues," *Physics Med. Biol.,* vol. 53, pp. 1773-1793, 2008.

[15]   S. A. Eyerly, S. J. Hsu, S. H. Agashe *et al.*, "An in vitro assessment of acoustic radiation force impulse imaging for visualizing cardiac radiofrequency ablation lesions," *Journal of Cardiovascular Electrophysiology,* vol. 21, pp. 557-563, 2010.

[16]   T. Varghese, U. Techavipoo, J. A. Zagzebski *et al.*, "Impact of gas bubbles generated during interstitial ablation on elastographic depiction of in vitro thermal lesions," *J Ultras Med,* vol. 23, pp. 535-544, 2004.

26

[17] M. Ribault, J. Y. Chapelon, D. Cathignol *et al.*, "Differential attenuation imaging for the characterization of high intensity focused ultrasound lesions," *Ultrasonic Imaging,* vol. 20, pp. 160-177, 1998.

[18] H. Zhong, M. X. Wan, Y. F. Jiang *et al.*, "Monitoring imaging of lesions induced by high intensity focused ultrasound based on differential ultrasonic attenuation and integrated backscatter estimation," *Ultrasound Med. Biol.,* vol. 33, pp. 82-94, 2007.

[19] S. Y. Zhang, M. X. Wan, H. Zhong *et al.*, "Dynamic changes of integrated backscatter, attenuation coefficient and bubble activities during high-intensity focused ultrasound (HIFU) treatment," *Ultrasound Med. Biol.,* vol. 35, pp. 1828-1844, 2009.

[20] A. Anand and P. J. Kaczkowski, "Monitoring formation of high intensity focused ultrasound (HIFU) induced lesions using backscattered ultrasound," *Acoustics Research Letters Online-ARLO,* vol. 5, pp. 88-94, 2004.

[21] B. A. Rabkin, V. Zderic, and S. Vaezy, "Hyperecho in ultrasound images of HIFU therapy: Involvement of cavitation," *Ultrasound Med. Biol.,* vol. 31, pp. 947-956, 2005.

[22] S. Vaezy, X. Shi, R. W. Martin *et al.*, "Real-time visualization of high-intensity focused ultrasound treatment using ultrasound imaging," *Ultrasound Med. Biol.,* vol. 27, pp. 33-42, 2001.

[23] X. Zheng and S. Vaezy, "An acoustic backscatter-based method for localization of lesions induced by high-intensity focused ultrasound," *Ultrasound Med Biol,* vol. 36, pp. 610-22, 2010.

[24] F. L. Lizzi, M. Astor, T. Liu *et al.*, "Ultrasonic spectrum analysis for tissue assays and therapy evaluation," *International Journal of Imaging Systems and Technology,* vol. 8, pp. 3-10, 1997.

[25]   R. H. Silverman, R. Muratore, J. A. Ketterling *et al.*, "Improved visualization of high-intensity focused ultrasound lesions," *Ultrasound Med. Biol.,* vol. 32, pp. 1743-1751, 2006.

[26]   S. Siebers, M. Schwabe, U. Scheipers *et al.*, "Evaluation of ultrasonic texture and spectral parameters for coagulated tissue characterization." pp. 1804-1807, 2004.

[27]   T. D. Mast, D. P. Pucke, S. E. Subramanian *et al.*, "Ultrasound monitoring of in vitro radio frequency ablation by echo decorrelation imaging," *J Ultras Med,* vol. 27, pp. 1685-1697, 2008.

[28]   T. D. Mast and S. Subramanian, "Analytic and numerical modeling of ultrasonic B-scan and echo decorrelation imaging," *Proceedings of Meetings on Acoustics,* vol. 9, pp. 020003, 2010.

[29]   C. C. Coussios, C. H. Farny, G. Ter Haar *et al.*, "Role of acoustic cavitation in the delivery and monitoring of cancer treatment by high-intensity focused ultrasound (HIFU)," *International Journal of Hyperthermia,* vol. 23, pp. 105-120, 2007.

[30]   F. L. Lizzi, "High-precision thermotherapy for small lesions," *Eur Urol,* vol. 23 Suppl 1, pp. 23-8, 1993.

[31]   C. H. Farny, R. G. Holt, and R. A. Roy, "The correlation between bubble-enhanced HIFU heating and cavitation power," *IEEE Trans Biomed Eng,* vol. 57, pp. 175-184, 2010.

[32]   T. D. Mast, V. A. Salgaonkar, C. Karunakaran *et al.*, "Acoustic emissions during 3.1 MHz ultrasound bulk ablation in vitro," *Ultrasound Med. Biol.,* vol. 34, pp. 1434-1448, 2008.

[33] J. McLaughlan, I. Rivens, T. Leighton *et al.*, "A study of bubble activity generated in ex vivo tissue by high intensity focused ultrasound," *Ultrasound Med. Biol.,* vol. 36, pp. 1327-1344, 2010.

[34] M. S. Canney, V. A. Khokhlova, O. V. Bessonova *et al.*, "Shock-induced heating and millisecond boiling in gels and tissue due to high intensity focused ultrasound," *Ultrasound Med. Biol.,* vol. 36, pp. 250-267, 2010.

[35] R. A. Roy, S. I. Madanshetty, and R. E. Apfel, "An Acoustic Backscattering Technique for the Detection of Transient Cavitation Produced by Microsecond Pulses of Ultrasound," *J Acoust Soc Am,* vol. 87, pp. 2451-2458, 1990.

[36] D. Melodelima, J. Y. Chapelon, Y. Theillere *et al.*, "Combination of thermal and cavitation effects to generate deep lesions with an endocavitary applicator using a plane transducer: Ex vivo studies," *Ultrasound Med. Biol.,* vol. 30, pp. 103-111, 2004.

[37] J. McLaughlan, I. Rivens, and G. ter Haar, "Cavitation detection in ex vivo bovine liver tissue exposed to high intensity focused ultrasound (HIFU)," in *2007 4th IEEE International Symposium on Biomedical Imaging: Macro to Nano Proceedings*, Arlington, VA, USA, 2007, pp. 1124-1127.

[38] C. H. Farny, R. G. Holt, and R. A. Roy, "Temporal and spatial detection of HIFU-induced inertial and hot-vapor cavitation with a diagnostic ultrasound system," *Ultrasound Med. Biol.,* vol. 35, pp. 603-615, 2009.

[39] V. A. Salgaonkar, S. Datta, C. K. Holland *et al.*, "Passive cavitation imaging with ultrasound arrays," *J Acoust Soc Am,* vol. 126, pp. 3071-3083, 2009.

[40] M. Gyöngy and C. C. Coussios, "Passive cavitation mapping for localization and tracking of bubble dynamics," *J Acoust Soc Am,* vol. 128, pp. E175-E180, 2010.

[41]   R. Otsuka, K. Fujikura, K. Hirata *et al.*, "In vitro ablation of cardiac valves using high-intensity focused ultrasound," *Ultrasound Med. Biol.,* vol. 31, pp. 109-114, 2005.

[42]   D. J. Engel, R. Muratore, K. Hirata *et al.*, "Myocardial lesion formation using high-intensity focused ultrasound," *Journal of the American Society of Echocardiography,* vol. 19, pp. 932-937, 2006.

[43]   R. Otsuka, K. Fujikura, Y. Abe *et al.*, "Extracardiac ablation of the left ventricular septum in beating canine hearts using high-intensity focused ultrasound," *Journal of the American Society of Echocardiography,* vol. 20, pp. 1400-1406, 2007.

[44]   K. Fujikura, R. Otsuka, A. Kalisz *et al.*, "Effects of ultrasonic exposure parameters on myocardial lesions induced by high-intensity focused ultrasound," *J Ultras Med,* vol. 25, pp. 1375-1386, 2006.

[45]   R. Muratore, Y. Abe, S. Homma *et al.*, "Cardiac ventricular HIFU: Convergence of experiment and theory in the canine model," in *6th International Symposium on Therapeutic Ultrasound*, Oxford, U.K., 2007, pp. 362-368.

[46]   D. J. Sahn, D. N. Stephens, J. M. Cannata *et al.*, "A family of intracardiac ultrasound imaging devices designed for guidance of electrophysiology ablation procedures," in *Proceedings of the 31st Annual International Conference of the IEEE Engineering in Medicine and Biology Society*, 2009, pp. 1913-1917.

[47]   M. Wright, E. Harks, S. Deladi *et al.*, "Real-time lesion assessment using a novel combined ultrasound and radiofrequency ablation catheter," *Heart Rhythm,* vol. 8, pp. 304-312, 2011.

[48] R. E. Kumon, Y. Zhou, K. Yang *et al.*, "Spectral analysis of ultrasound backscatter for characterization of HIFU lesions in cardiac tissue with high-frequency imaging," in *2009 IEEE International Ultrasonics Symp. Proc.*, Rome, Italy, 2009, pp. 244-247.

[49] T. Fawcett, "ROC Graphs: Notes and practical considerations for researchers," Tech Report HPL-2003-4, HP Laboratories 2004, http://www.hpl.hp.com/personal/Tom_Fawcett/papers/index.html.

[50] C. Kasai, K. Namekawa, A. Koyano *et al.*, "Real-time two-dimensional blood-flow imaging using an auto-correlation technique," *IEEE Transactions on Sonics and Ultrasonics,* vol. 32, pp. 458-464, 1985.

[51] T. J. Hall, E. L. Madsen, F. Dong *et al.*, "Low-reflection-coefficient liquid interfaces for system characterization," *Ultrasound Med. Biol.,* vol. 27, pp. 1003-1010, 2001.

[52] J. Kushibiki, N. Akashi, T. Sannomiya *et al.*, "Vhf Uhf Range Bioultrasonic Spectroscopy System and Method," *Ieee T Ultrason Ferr,* vol. 42, pp. 1028-1039, 1995.

[53] J. M. M. Pinkerton, "The Absorption of Ultrasonic Waves in Liquids and its Relation to Molecular Constitution," *Proc. Phys. Soc. B,* vol. 62, pp. 129–141, 1949.

TABLE 1

Results from pixel-by-pixel lesion classification for different parameters.

Parameter	Area Under Curve ($\mu \pm \sigma$)	Optimal Threshold	Accuracy	Sensitivity	Specificity
IBS_{max} (dB)	0.96 ± 0.02	12.0	0.94	0.76	0.98
ΔM_{max} (dB)	0.95 ± 0.04	15.8	0.93	0.79	0.97
ΔI_{max} (dB)	0.91 ± 0.06	25.5	0.91	0.68	0.97
$\sigma_{FF, max}$	0.93 ± 0.05	1.28	0.92	0.66	0.98
$\sigma_{IF, max}$	0.91 ± 0.05	1.48	0.91	0.57	0.99
Grayscale (dB)	0.68 ± 0.08	0.75	0.84	0.20	0.98
Δm_{max} (dB/MHz)	0.52 ± 0.11	0.49	0.79	0.8	0.97

TABLE 2

Comparison of predictive parameters of training, test and entire datasets for lesion identification

in percentages using temporal maximum integrated backscatter with a threshold of 12 dB.

Dataset	Accuracy	Sensitivity	Specificity
Training	0.94	0.76	0.98
Test	0.93	0.73	0.98
All Data	0.94	0.76	0.98

FIGURE CAPTIONS

Figure 1. Experimental setup of image-guided HIFU system (not to scale).

Figure 2. (A) Block diagram of procedure for obtaining the binary mask of lesion in gross image. (B) Manually drawn outer edge of the lesion (cyan) in gross image. (C) Registration of STBM window location (white dashed lines) in B-mode image. (D) Spotted STBM window location on gross image after overlaying Fig. 2C on Fig. 2B. (E) The binary mask of lesion obtained from gross image in Fig. 2D **(Media-Color 1)**.

Figure 3. Grayscale B-mode images (A) before and (B) after HIFU with dash-dotted lines showing the location of the Short-Time B-Mode (STBM) window that was used for image during HIFU at a frame rate of 77 Hz, intensity of 2600 W/cm^2, 50% duty cycle, and 1 s exposure time. The direction of HIFU beam was from left to right. (C) Post-HIFU photograph of lesion and cavity in gross tissue specimen. (D) Horizontally-stacked STBM grayscale frames showing the spatiotemporal evolution of the lesion in the STBM window. Vertical dash-dotted lines indicate the times when the HIFU was turned on and off. (E) Photograph of lesion and cavity in gross tissue specimen, rescaled to have the same spatial scale as Fig. D. The contour on the outer edge of the lesion has been marked (cyan), and the location of STBM window lines is shown by the white dashed lines. The dashed yellow lines show correspondence between features in ultrasound and optical images. (F) Selected individual STBM grayscale frames before (F_1), during (F_2–F_7), and after (F_8–F_{11}) application of HIFU **(Media-Color 2)**.

Figure 4. Comparison of overall ROC curves for several methods in detecting the lesion for all specimens (IBS$_{max}$: temporal maximum (t.m.) of integrated backscatter, ΔM_{max}: t.m. of relative change in mid-band fit, ΔI_{max} : t.m. of relative change in intercept, $\sigma_{FF,max}$: t.m. of frame-to-

34

frame decorrelation, $\sigma_{IF,\max}$: t.m. of initial frame decorrelation, and GS: Grayscale) **(Media-Color 3)**.

Figure 5. (A) Stacked short-time B-mode (STBM) grayscale frames with marked regions of gas-body activity (green pixels) of dataset with macroscopic cavity (data in Figs. 3). The top most green pixel in each frame is marked by a red dot. Vertical dash-dotted lines indicate the times when the HIFU was turned on and off. (B) Gross image of dataset in (A) with lesion contour (cyan) and location of STBM window lines (vertical white dashed lines) (C) STBM grayscale frames with marked regions of gas-body activity of dataset without macroscopic cavity (D) its gross image. (E) Position of uppermost gas-body activity in the cavity dataset (Fig. 5A), non-cavity dataset (Fig. 5C) and their corresponding moving average (dashed lines) based on a averaging window of 0.08 s. (F) Expansion rate of gas-body activity from numerical derivatives of curves in Fig. 5A **(Media-Color 4)**.

Figure 6. Expansion rate of non-cavity ($n = 5$) and cavity ($n = 19$) datasets with error bars. The selected expansion rate threshold (0.8 mm/s) is shown by the dot-dashed horizontal line.

Figure 7. Example of lesion with gas-body activity and cavity formation (2600 W/cm^2, 77 Hz PRF, 50% duty cycle and 1 s exposure time). The time evolution of ablation process is shown at selected times. The green frame labels indicate the frames during HIFU exposure. The area of tissue necrosis evaluated using the optimal $IBS_{\max}$ threshold of 12 dB is represented in red, gas bodies expanding at less than expansion rate threshold (<0.8 mm/s) in green, and gas bodies which crossed expansion rate threshold in blue ($\geq$0.8 mm/s). The lesion contour in each frame is shown in cyan **(Media-Color 5)**.

Figure 8. Example of lesion with gas-body activity and cavity formation (2600 W/cm^2, 130 Hz PRF, 50% duty cycle and 1 s exposure time). (A) B-mode image after HIFU treatment with

location of STBM window shown by the dashed vertical lines (white). (B) Image of gross tissue with lesion, manually estimated lesion contour (cyan), and location of STBM window (vertical dashed green lines). (C) B-mode image with an overlay of predicted lesion (red) using IBS_{max} in STBM window and manually estimated lesion contour (cyan) from gross image. (D) Time evolution of ablation process is shown at selected times (see Fig. 7 caption for description of colors) **(Media-Color 6)**.

Figure 9. Example of lesion with gas-body activity but without macroscopic cavity formation (2600 W/cm^2, 77 Hz PRF, 50% duty cycle and 0.2 s exposure time). (A) B-mode image after HIFU treatment with location of STBM window shown by the dashed vertical lines (white). (B) Image of gross tissue with lesion, manually drawn lesion contour (cyan), and location of STBM window (vertical dashed green lines). (C) B-mode image with an overlay of predicted lesion (red) using IBS_{max} in STBM window and manually estimated lesion contour (cyan) from gross image. (D) Time evolution of ablation process is shown at selected times (see Fig. 7 caption for description of colors) **(Media-Color 7)**.
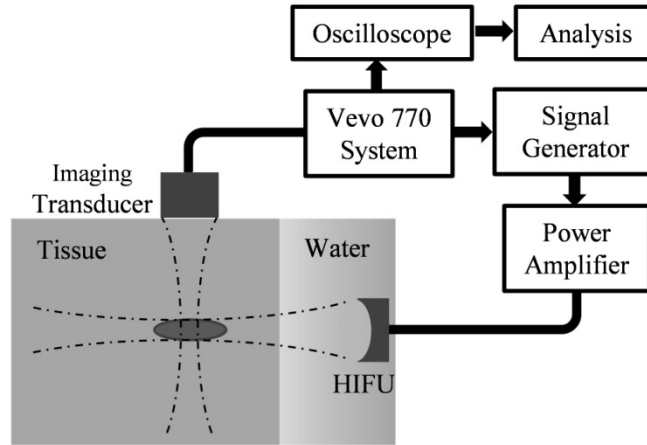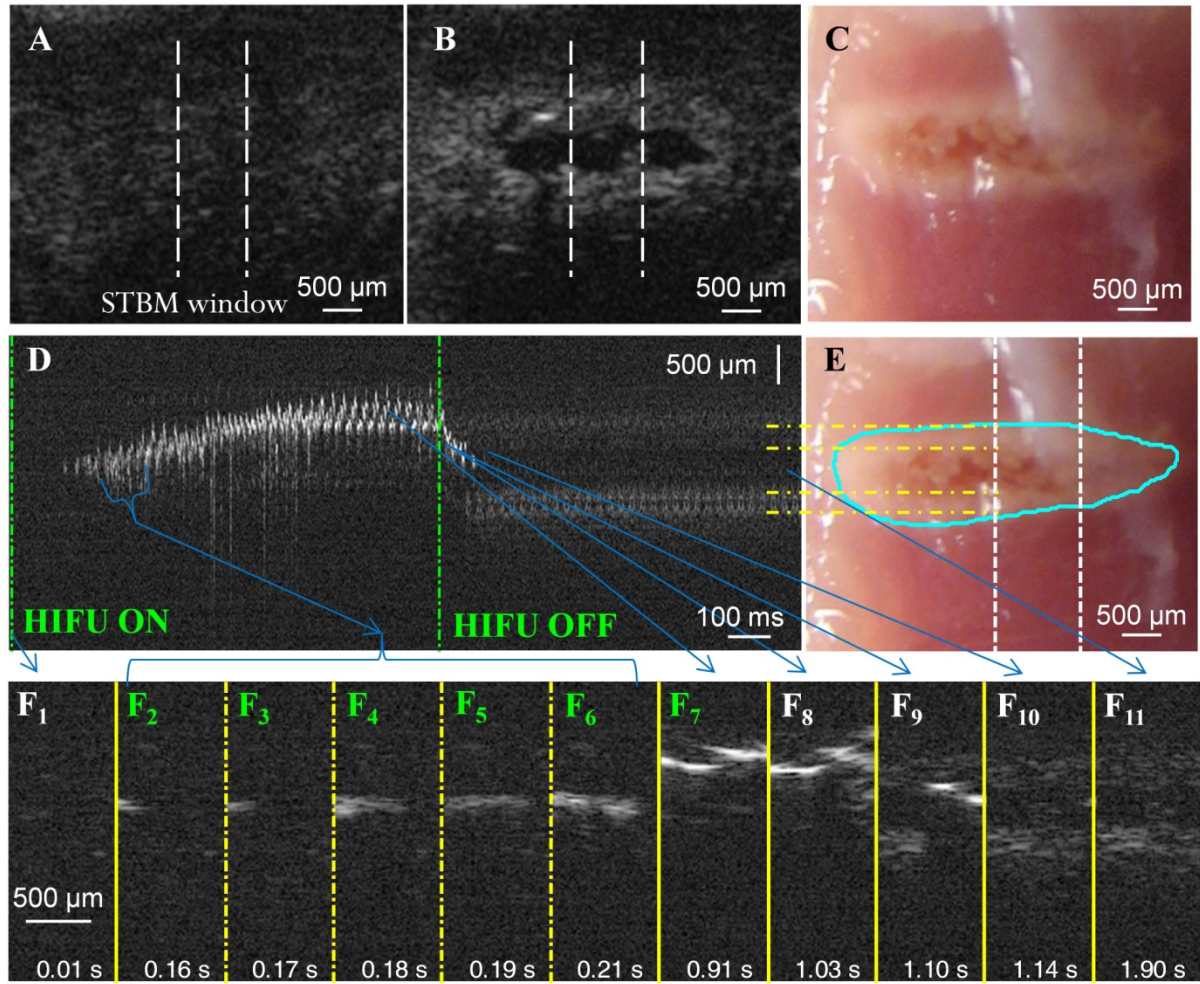
Figure 1
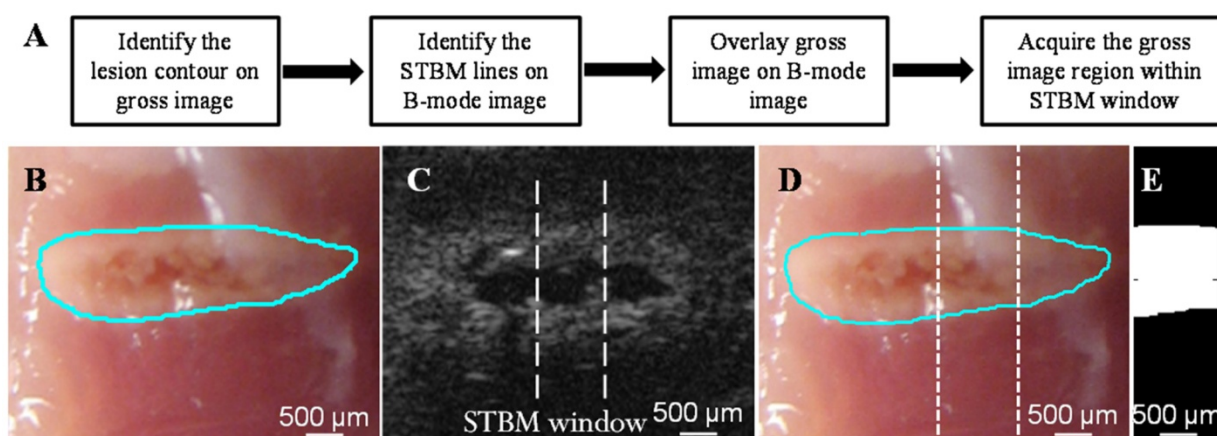
Figure 2 (color online)
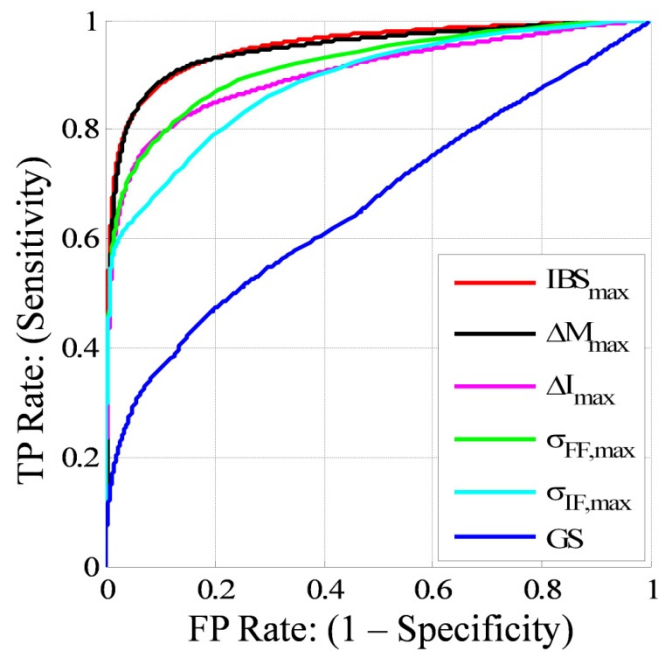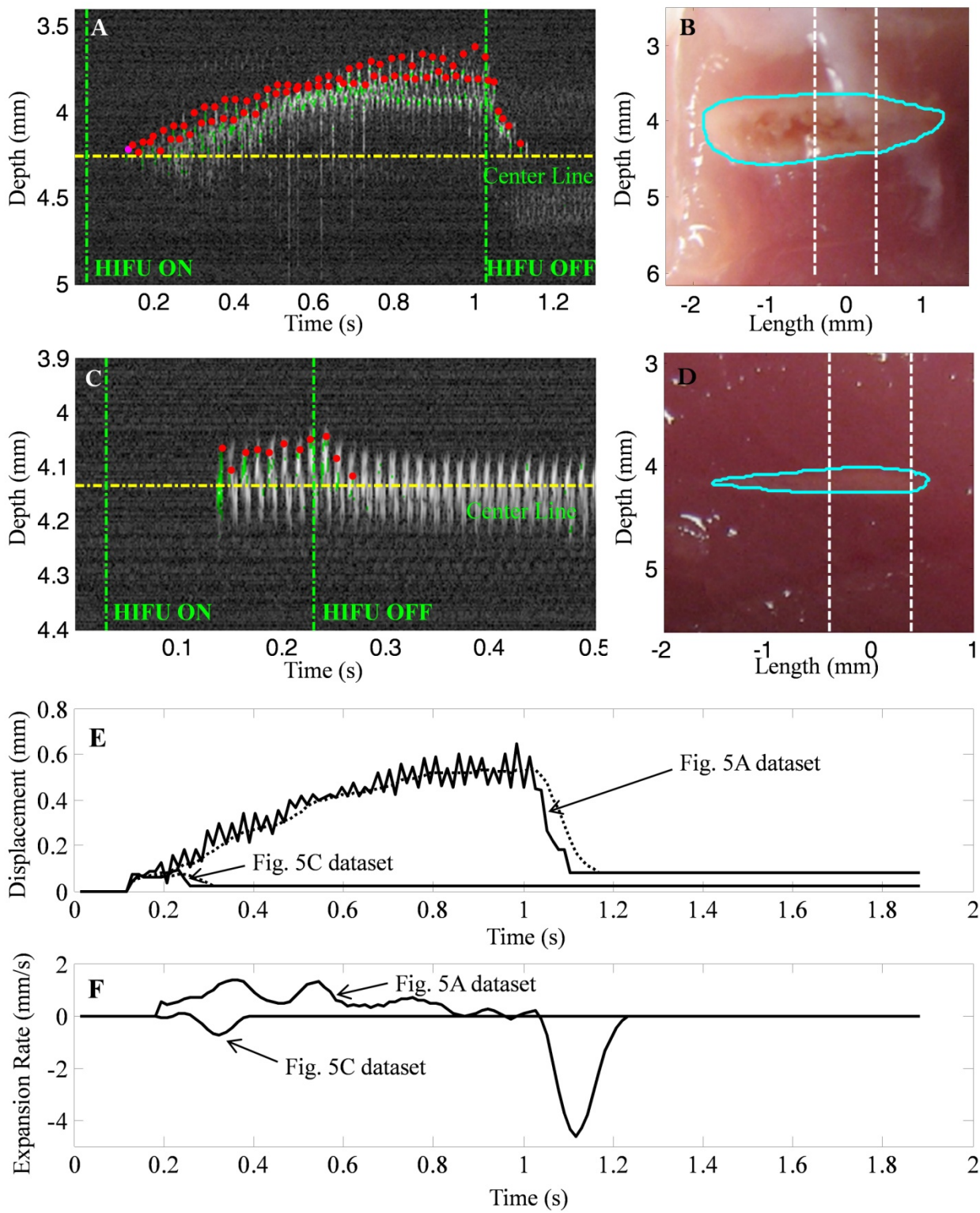
Figure 3 (color online)

Figure 4 (color online)
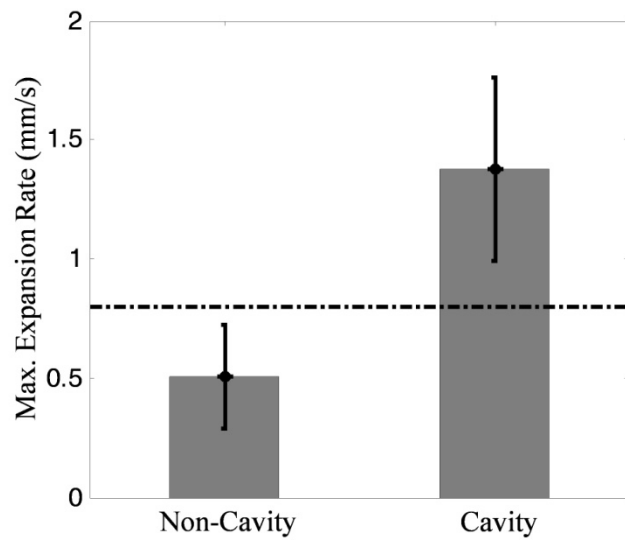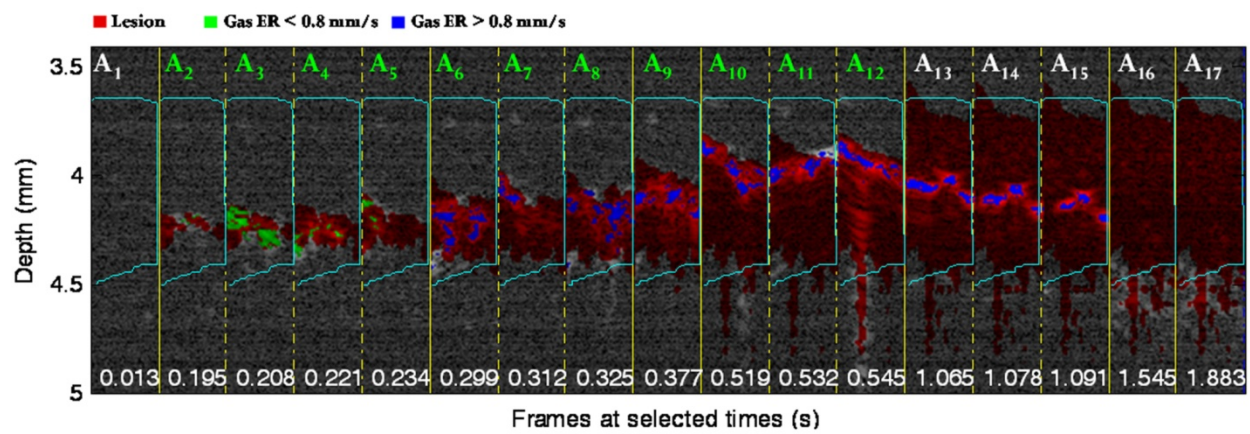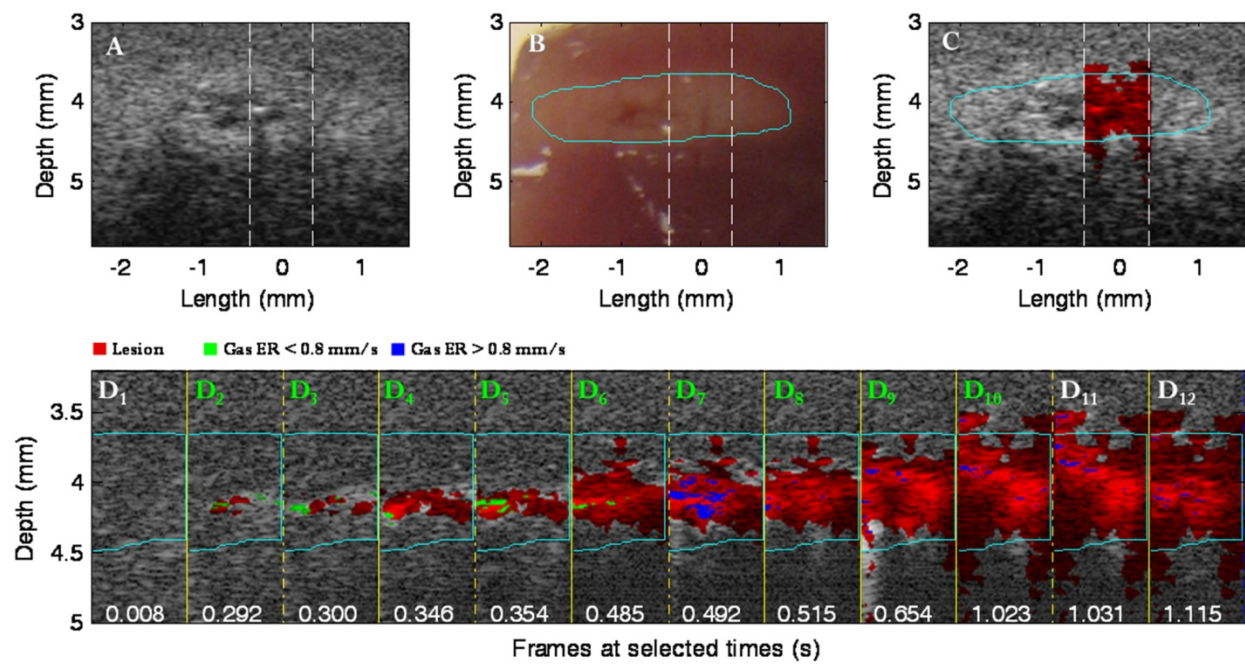
Figure 5 (color online)
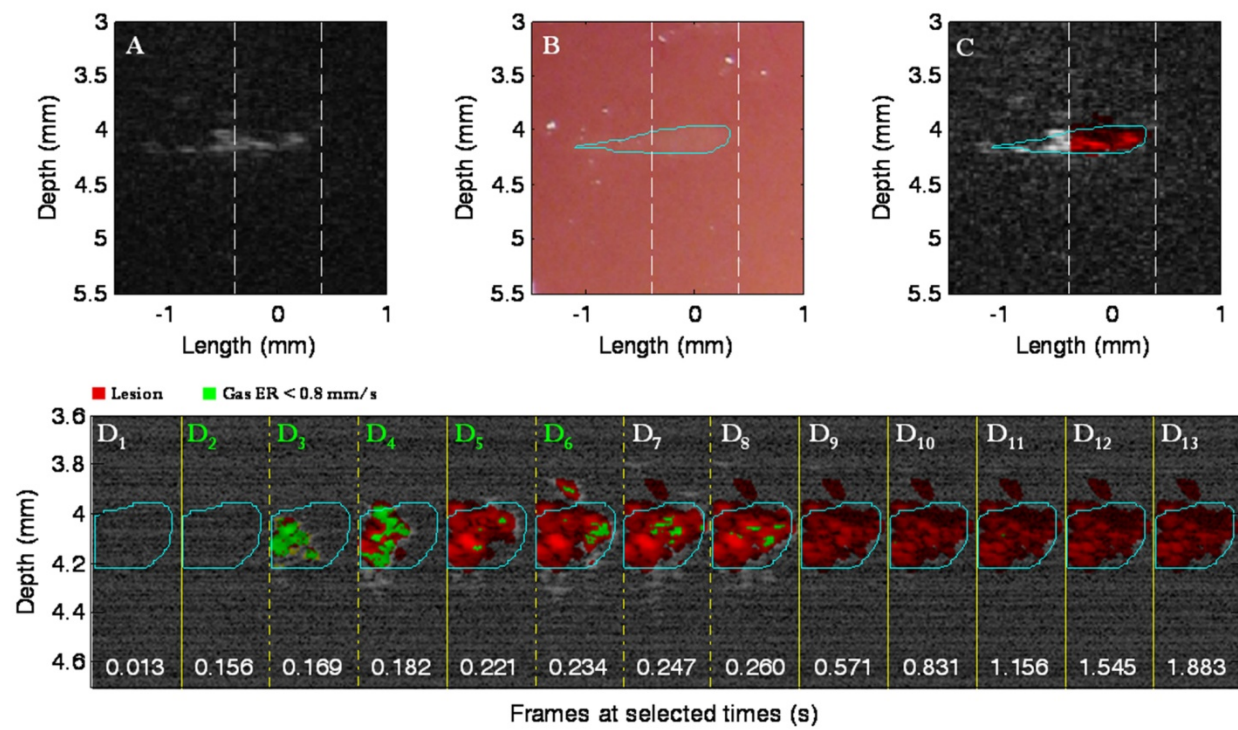
Figure 6

Figure 7 (color online)

Figure 8 (color online)

Figure 9 (color online)